Wave Transformation and Air Entrainment by a Harmonically Forced Plunging Jet

Sophia T. L. Relph[1,*], Kenneth T. Kiger[2]

1: Dept. of Mechanical Engineering, The University of Maryland, College Park, USA
2: Dept. of Mechanical Engineering, The University of Maryland, College Park, USA
*Corresponding author: relph@umd.edu

Keywords: Air entrainment, Harmonic forcing, Background oriented schlieren, Free surface flows, Metal casting

ABSTRACT

It is known that air may be entrained by a plunging jet even when that jet is relatively small and slow, so long as it has significant disturbances (Zhu et al., 2000). In the current work, harmonic disturbances of controlled frequency and amplitude are used to produce air entrainment. At sufficient frequency and amplitude, the harmonic jet disturbances cause azimuthal subharmonic waves on the plunge pool surface to appear, oscillating at half of the forcing frequency. These subharmonic waves interact with the jet flow to entrain air at lower disturbance amplitudes and jet velocities than previously documented. The dependence of the wave shape and inception criteria on jet parameters, namely frequency and diameter, is investigated, giving results that agree well with past investigations of azimuthal waves driven by surface-piercing bodies. The number of azimuthal wave lobes may be understood as the ratio of the perimeter length of the forced jet and the wavelength of the resulting azimuthal water waves, given by $n_{\text{waves}} = Ck_{f/2}r_{\text{j}}$, where C is the ratio of the wave and jet diameters. In past experiments, C was approximately 1.2, but with much smaller liquid jets, we found that C can be as high as 1.4-2 (Shen & Liu, 2020). The volumetric flow rate of entrained air was measured directly, by way of a capture hood, enabling investigation of air entrainment behavior, and it is concluded that the resultant air flow rate is dependent on several factors, including jet frequency, azimuthal wave mode number, jet velocity, and the jet disturbance amplitude. The influence of several of these factors was determined by the use of an effective bubble size parameter, hypothesizing that every wave trough during every wave cycle was equally likely to entrain air, an assumption that appears borne out in fact. This effective bubble size, free of the influences of forcing frequency and wave mode number, was found to depend on the forcing intensity in an approximately linear fashion, at least for forcing amplitudes close to those required for entrainment inception. Jet and wave measurements were conducted using high speed videography, enabling quantitative measurements of the near-jet wave amplitude, as well as the size and spectral nature of the jet disturbances.

1. Introduction

Metal casting is ubiquitous in modern industry, and its products are relied upon in all facets of modern life. Of paramount importance in this discipline is the minimization of air entrainment

events, in which the act of pouring a casting causes pockets of air to be entrapped within the melt, weakening parts and impacting their longevity (Ridgeway et al., 2020). These events therefore must be well understood, but the existing literature concerning air entrainment exhibits uncertainty concerning the mechanisms and conditions of air entrainment. This work addresses that uncertainty with a novel jet forcing approach where jet conditions, particularly surface disturbances, can be repeatably imposed. Air entrainment behavior is observed to depend strongly on jet disturbances, and that dependence has been documented as affecting air entrainment rate, conditions, and mechanisms.

The existing literature on air entrainment by plunging jets concludes that as a rule, air entrainment rate increases with the disturbance level of the jet. However, existing works focus on naturally evolving disturbances, both due to jet instabilities and the decay of turbulent nozzle exit conditions, which then creates relatively complex and poorly controlled conditions at the impact site, conflating the effects of diameter, disturbance amplitude and disturbance frequency (Davoust et al., 2002). This motivates the current work, wherein a well-conditioned plunging jet has disturbances imposed on it by vibrating the emitting nozzle. By varying the characteristics of the forcing vibrations, the jet's disturbances can be adjusted in amplitude and frequency, allowing the disturbance state of the jet to be precisely controlled.

We have found that in the case of higher frequency jet disturbances (above approximately 30 Hz for the size jets studied in this work), the typically symmetric and concentric waves generated by the jet on the surface of the plunge pool can transition into a radially symmetric, subharmonic, azimuthal wave mode, provided there is a sufficient disturbance intensity. When this happens, it appears that the meniscus between the jet and plunge pool destabilizes, with the azimuthal waves emitting from it as in Fig. 1.

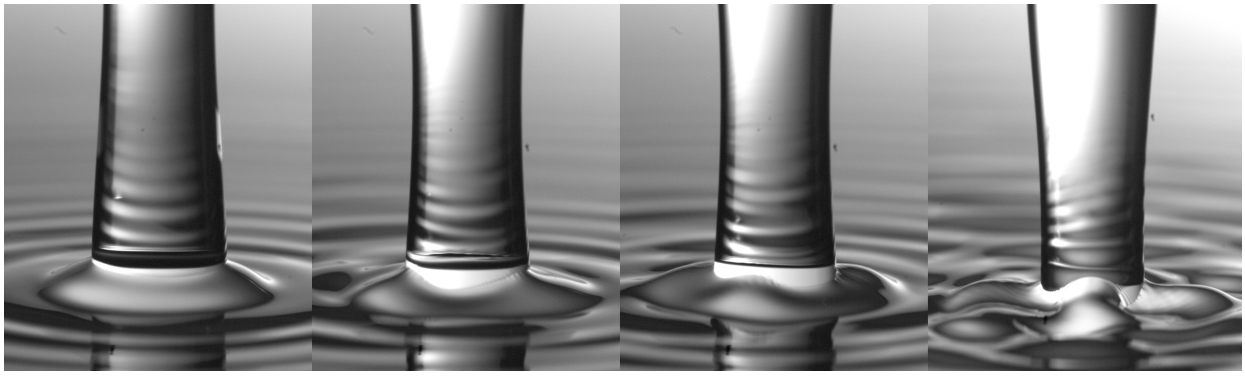

Figure 1. A time series showing the onset of azimuthal waves. At left, the jet forcing has begun, but the meniscus and surface waves remain axisymmetric. In the second and third images, taken one disturbance cycle apart, radially-symmetric azimuthal waves have emerged from the previously axisymmetric meniscus. In the final image, the waves have become as large as the meniscus itself. The jet is being forced at a frequency of 60 Hz, and its diameter and impact velocity are 7.6 mm and 2.5 m/s, respectively.

Furthermore, if driven strongly enough, the jet-driven azimuthal waves can initiate air entrainment, as the troughs deepen and subsequently interact with the subsurface jet flow. These entrain-

ment events typically begin with a wave trough getting pinched downwards, before expanding significantly underwater, as pictured in Fig. 2. We suspect that the bubble expands fastest and widest as it reaches the core of a ring vortex controlled by the jet momentum flux and disturbance intensity; this may also interact with disturbance-driven Kelvin-Helmholtz vortex shedding as described by Becker & Massaro (1968).

In the course of these investigations, it has been noted that azimuthal wave air entrainment events occur at jet velocities and disturbance intensities that would not result in air entrainment by previously documented mechanisms. Further investigation of these jet-driven subharmonic waves is therefore required to more completely understand air entrainment by plunging jets.

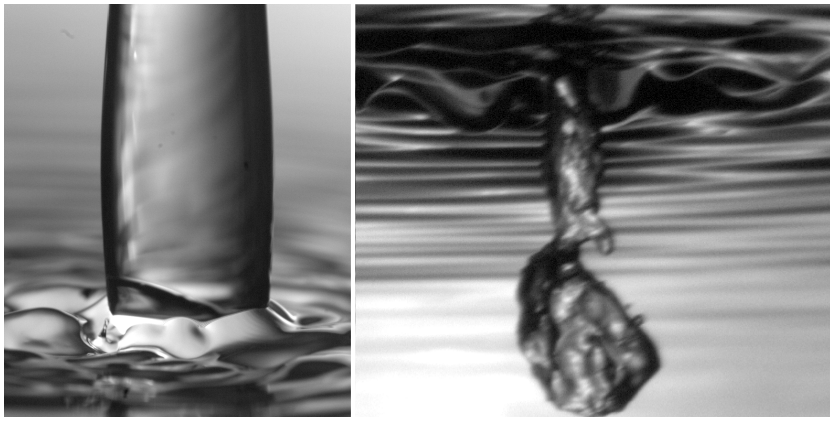

Figure 2. Air entrainment by azimuthal waves, for a case with 80 Hz jet forcing, 8.7 mm impact diameter, and 3.1 m/s impact velocity. One of the wave troughs has become drawn down by subsurface flow, causing it to mushroom out into a bubble.

The subharmonic azimuthal waves bear a strong resemblance to those discussed in investigations by Tatsuno et al. (1969), in which a semi-immersed solid sphere was vibrated vertically, and caused the waves around it to transition from concentric to azimuthal patterns. Tatsuno et al. found that the required disturbance amplitude for the waves to transition varied with the frequency, as did the degree of symmetry of the waves themselves, a behavior also noted here. However, because those studies were performed with impermeable objects for surface forcing, rather than a disturbed liquid jet, they did not consider any regime susceptible to air entrainment, and the topic has been largely unstudied since. Here, the addition of the plunging jet adds a new element to the wave dynamics: the presence of the subsurface free jet flow. Taneda (1991) found that oscillating spheres and their subharmonic azimuthal waves can drive subsurface flows, but these are much different from the flow imposed by the momentum flux of a plunging jet. As such, it remains to be seen precisely how these azimuthal waves interact with a flow like the turbulent submerged jet beneath the plunge point.

2. Experimental approach

To generate a jet with well-characterized disturbances, a nozzle vertically oscillated by mounting it to low-friction air bearings driven by voice coil actuators. The low-friction, linear motion, as well as driving actuators, result in repeatable nozzle motions. The nozzle outflow velocity is determined using a Coriolis flow meter, and the nozzle motion is measured using a PCB Piezotronics 356A16 accelerometer, which, combined with the datalogging system, has a minimum reading of 0.12 ms^{-2} and a maximum range of ± 490 ms^{-2}. A NI USB-6001 multifunction IO device is used for logging accelerometer data as well as generating the nozzle forcing signals and camera/data acquisition synchronization signals.

The nozzle itself is shaped using an axisymmetric converging section that is fed by a plenum and turbulence mitigation section. Fluid from the plenum passes through a bed of 3 mm glass beads, as well as a fine mesh screen, to even out the flow and prevent any circulation in the plenum from affecting the jet. The converging section of the polished acrylic nozzle is a spline curve designed to prevent flow separation, as described by Morel (1975), and three different nozzles are used with diameters of 5 mm, 10 mm, and 20 mm, respectively.

At present, the conditions studied vary the forcing frequency between 10 and 200 Hz. Three impact velocities are used; 2.1, 2.5, and 3.1 m/s, which together with the available nozzle diameters result in a range of impact Reynolds numbers between approximately 9×10^3 and 4×10^4. These velocities are low enough that the jets do not entrain air when unforced, meaning that all air entrainment events that occur are a result of the imposed disturbances.

The cameras employed are Phantom High Speed cameras, models VEO640L and V641, recording at a typical frame rate of 1000 frames per second. Both cameras are capable of a maximum resolution of 2560x1600 pixels. One is used for measuring the jet disturbances over time by extracting a row of pixels from high-speed video to determine the locations of the jet edges. This allows for the evolution of the jet shape over time to be determined, as well as its spectral components. At high frequencies and low amplitudes, the temporal evolution of the jet disturbances approximates that of a sine wave, but at low frequencies, and therefore longer disturbance wavelengths, capillary effects the cylindrical geometry distort the trend into an approximate sum of sines. To characterize the intensity of the disturbances, we take the difference of the maximum and minimum diameters of the jet, such that the disturbance amplitude at a given state of forcing would be described by the frequency and the dimensional size of the disturbances. Additionally, in order to observe all of the azimuthal waves simultaneously, it was necessary to view the jet from directly beneath; this was accomplished by using a high speed camera and an underwater mirror, to give a vertical viewing aspect, visible in Fig. 4.

While direct observations with high-speed videography allow for the identification of the physical processes by which disturbed plunging jets entrain air, these observations are fundamentally limited without the ability to also measure the relevant air flow rate. The measurement of this parameter is technically challenging, however, as the measurement scheme needs to accurately and

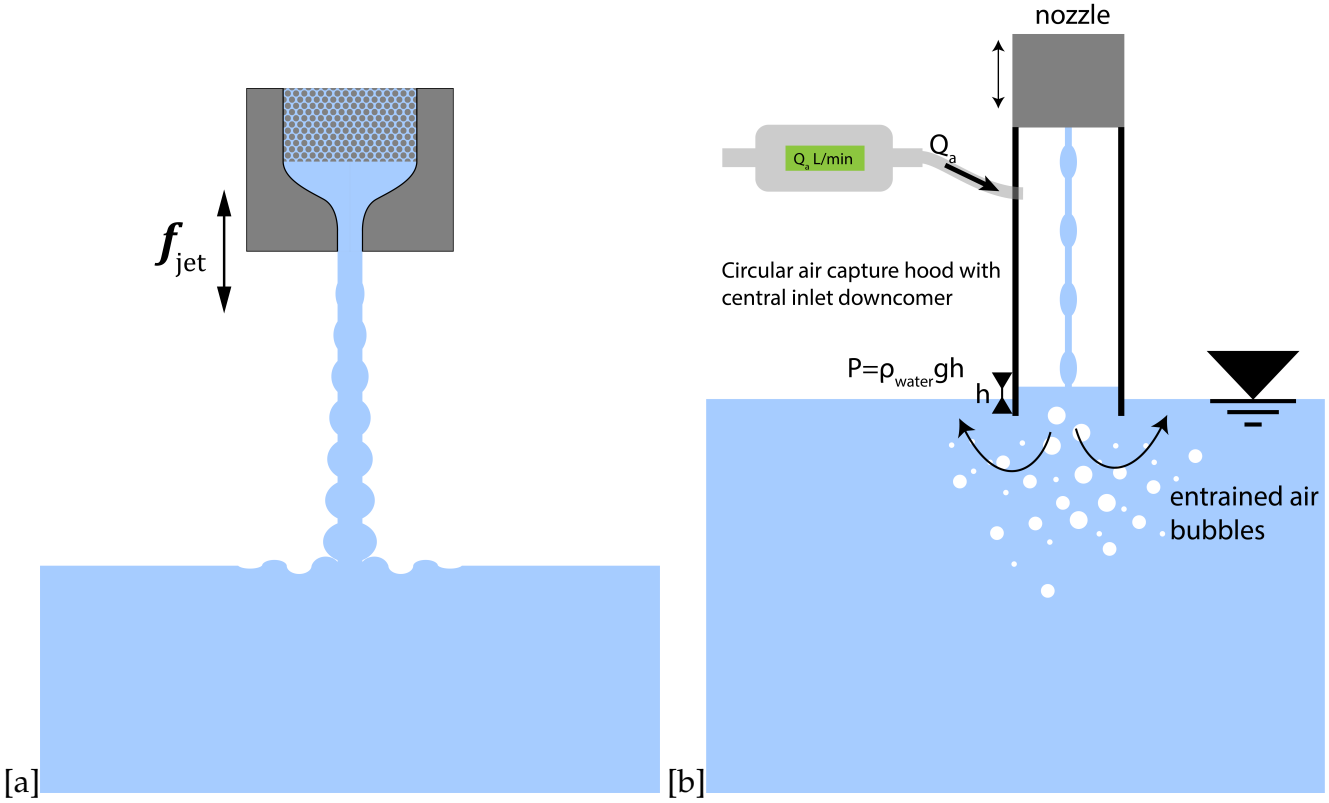

Figure 3. (a) The forced plunging jet arrangement (b) The air capture system

reliably capture the majority of the entrained air volume without interfering substantially with the air entrainment process. In this work, it was decided to measure the volumetric flow rate of entrained air by segregating the captured bubbles and measuring the rate of air drawn into the region surrounding the jet, rather than attempting to use visual or void fraction-based methods. For air entrainment measurements, the jet is enclosed in a 50 mm diameter downcomer tube as depicted in Fig. 3, which extends from the nozzle down to approximately 10 mm below the surface of the receiving pool, thusly creating a closed air volume. Bubbles are first captured within the pool, then carried outwards by the subsurface flow, surfacing outside of the downcomer and thereby extracting air out of it. Air extracted from the downcomer by bubble entrainment is replaced through an inlet tube, to which is connected a thermal mass flow meter. The nozzle is connected to the stationary downcomer tube by way of a flexible bellows, allowing it to vibrate and impose jet disturbances while still sealing the downcomer space. The primary drawback of such a configuration is that as the nozzle vibrates, its motion can induce very small net air volumes to enter and exit the downcomer by way of the flow meter, resulting in artificially elevated flow rate measurements. To correct for this, flow rate data was collected twice for each disturbance case; once with the jet running, and once with the nozzle plugged and jet absent, but the downcomer still connected and sealed. By subtracting the mean no-jet flow rate from the running jet flow rate and setting a threshold value below which the flow rate is considered to be zero, we discriminate the air flow rate from non-entraining conditions and also compensate for the motion of the nozzle. However, it should be mentioned that the motion of the nozzle is not the only factor that can alter the enclosed

volume of the downcomer; the pressure fluctuations created by nozzle motion, as well as the jet disturbances, can both cause the free surface height inside the downcomer to fluctuate, typically on the order of millimeters in places, potentially inducing some erroneous components still remaining in the flow rate measurements. Future investigations of this phenomenon using this type of air capture apparatus would likely benefit from a substantially larger downcomer volume, in order to reduce the impact of such flow rate errors.

To investigate the effect of the relevant jet parameters on air entrainment, namely the impact velocity, impact diameter, forcing frequency, and forcing amplitude, we ran the three available jet nozzles at three different velocities; because of the acceleration of the jet due to gravity, we can vary the jet diameter not only by using larger nozzles, but also by changing the flow rate or drop height. In this early work, the nozzle mean elevation was not changed, permitting the use of a single downcomer. In addition, the largest diameter achievable with a given nozzle size is close to the smallest jet diameter achievable with the next largest nozzle; We can therefore determine the effect of jet speed on air entrainment performance, while keeping the diameter mostly constant. Accordingly, we can investigate the effect that both diameter and velocity have on air entrainment and free surface behaviors, though not independently without also varying the drop height. The parameters of the seven jet cases are described in Table 1.

Table 1. Operational parameters of different jet conditions. By altering the flow rate and nozzle diameter, a wide variation in impact velocity may be accomplished without significantly changing impact point diameter. The different values of L_j are due to different converging nozzle dimensions. An impact velocity of 2.4 m/s rather than 2.5 was used in the "20mm normal" case to prevent undesired air entrainment events; due to nozzle flow conditions, a flowrate any higher would have resulted in unacceptable levels of unforced jet disturbances.

	D_0 (mm)	L_j (mm)	D_j (mm)	U_j (m/s)
5mm normal	5	207	3.9	2.5
5mm high	5	207	4.4	3.1
10mm low	10	212	4.9	2.1
10mm normal	10	212	7.6	2.5
10mm high	10	212	8.7	3.1
20mm low	20	187	9.8	2.1
20mm normal	20	187	15.5	2.4

3. Results

At sufficient driving frequency and amplitude, the surface around the base of the jet destabilizes, transitioning from only ring waves to an azimuthal wave pattern that oscillates at half of the jet frequency. It was determined that different driving frequencies result in different mode shapes, or the degree of rotational symmetry of the subharmonic waves, much like in the hard sphere case. As demonstrated in Fig. 4, the wave mode number n_{waves} can be varied by altering the forcing

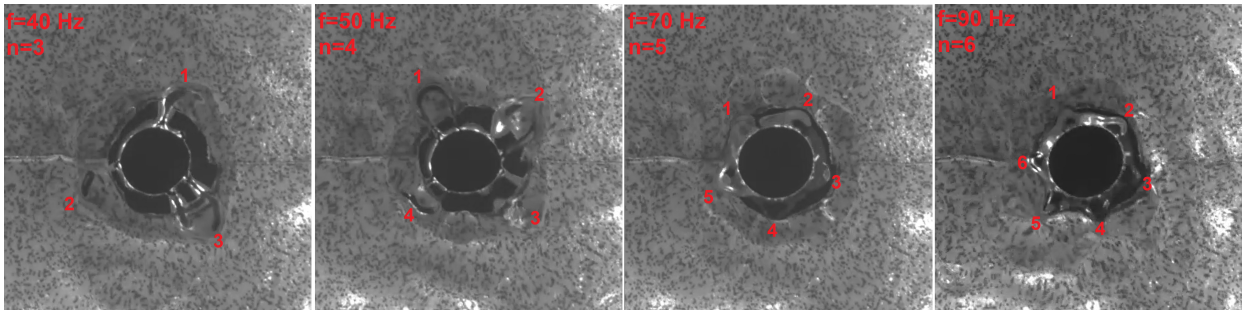

Figure 4. Wave shapes for 3, 4, 5, and 6 lobe cases, looking vertically up at the jet from the bottom of the plunge pool. The dotted background is an optical target for a background-oriented schlieren surface measurement technique developed by Moisy et al. (2009).

frequency, with given examples illustrating n_{wave} = 3, 4, 5 and 6. The selection of this number is assumed to come as a result of the subharmonic waves' gravity-capillary wavelength being close to an integer fraction of a circumferential length around the perimeter of the jet. Thusly, higher frequencies will return a smaller wavelength, thereby increasing n_{waves}, and a larger jet diameter will result in a greater perimeter length, also increasing n_{waves}. Fig. 5 maps out the variation of observed n_{waves} values with different jet diameters and frequencies, illustrating how the wave mode depends on both parameters. Additionally, it can be seen that the mode shapes observed were no higher than $n_{\text{waves}} = 20$ and no lower than $n_{\text{waves}} = 3$. The upper limit of n_{waves} is purely determined by the limits of the forcing that was applied; frequencies higher than 200 Hz could have been studied, but were considered outside the scope of the present work, while the lower limit was imposed by physical constraints; it would be prohibitively difficult to identify azimuthal waves with n_{waves} equal to 2 or 1.

For predicting the wave mode number, we use the gravity-capillary dispersion relation:

$$\omega^2 = |k| \left(\frac{\rho_w - \rho_a}{\rho_w + \rho_a} g + \frac{\sigma}{\rho_w - \rho_a} k^2 \right) \tag{1}$$

This allows us to determine the angular wavenumber of the subharmonic azimuthal waves as a function of frequency, effectively:

$$\frac{2\pi}{\lambda_{f/2}} = k_{f/2} = k(\omega_{\text{jet}}/2) \tag{2}$$

Furthermore, it is assumed that the number of lobes in the azimuthal wave ring is a result of the ratio between the perimeter of the wave ring and the expected wavelength based on the subharmonic frequency, $\lambda_{f/2}$:

$$n_{\text{waves}} = \frac{\pi D_{\text{waves}}}{\lambda_{f/2}} = \frac{D_{\text{waves}} k_{f/2}}{2} = r_{\text{waves}} k_{f/2} \tag{3}$$

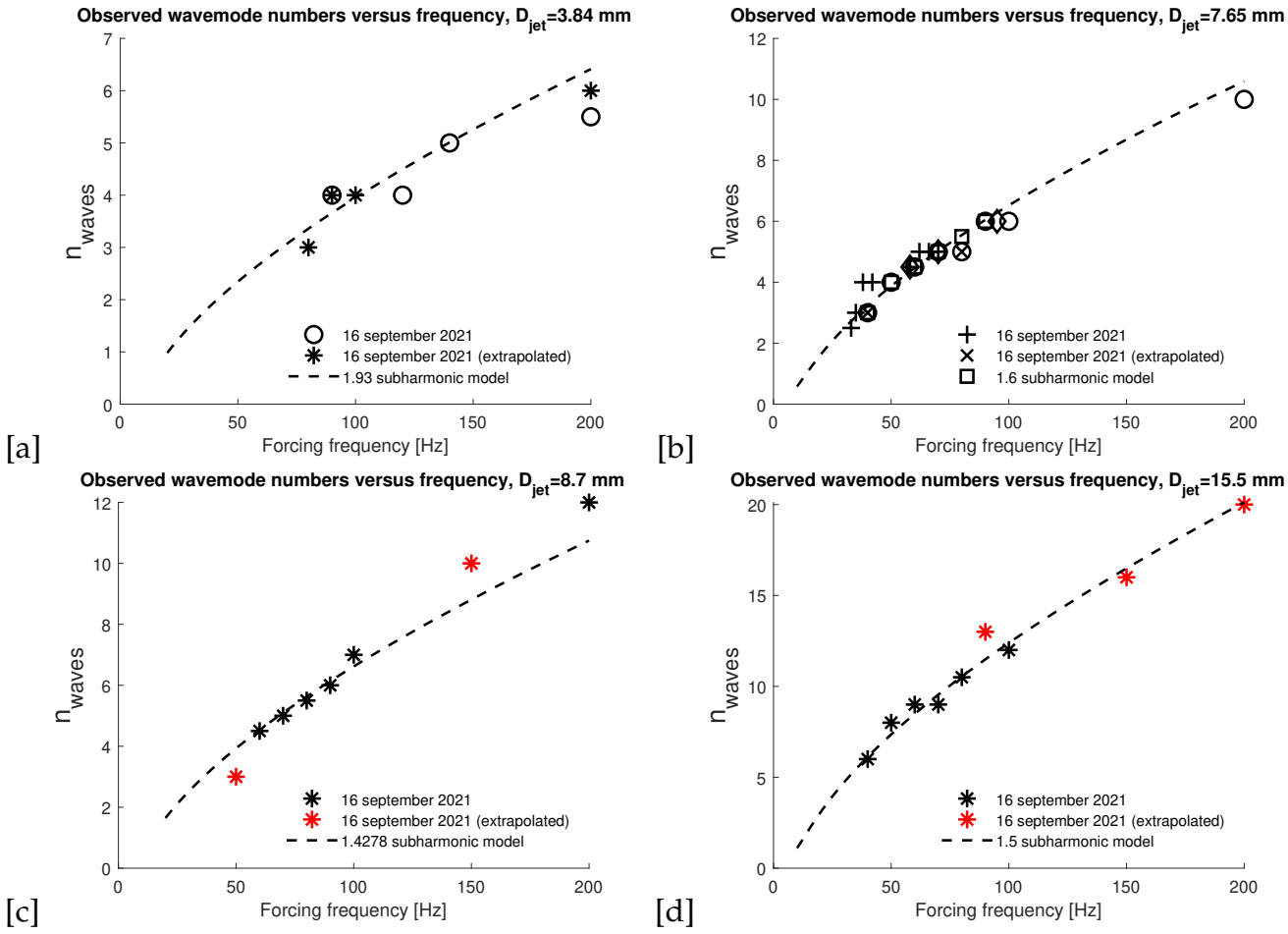

Figure 5. n_{waves} versus forcing frequency, for selected jet cases. (a) 5mm 2.5m/s (b) 10mm 2.5m/s (c) 10mm 3.1m/s (d) 20mm 2.4m/s. "Extrapolated" values of n_{waves}, marked in red, come from cases where unforced non-axisymmetric jet disturbances were strong enough to partly disrupt the formation of the azimuthal waves, with the waves only forming on a part of the jet perimeter.

Tatsuno et al. (1969) supposed that the diameter of the wave ring, D_{waves}, must be larger than that of their sphere, which in our case would correspond to the jet impact diameter, D_j. Therefore, the number of waves around the perimeter of the jet should be described as:

$$n_{\text{waves}} = \frac{D_{\text{waves}}}{D_{\text{j}}} k_{f/2} r_{\text{j}} \tag{4}$$

Knowing the driving frequency, we may compute the expected wavelength of the resultant surface waves, and therefore the expected number of wave lobes, and it is straightforward to determine a D_{waves}/D_j ratio that fits best. In the past, investigations of azimuthal waves driven by surface-piercing hard spheres, particularly those by Tatsuno et al. (1969) and Shen & Liu (2020), found a constant diameter ratio of 1.2. Fig. 6 illustrates the variation of the diameter ratio in the present study, indicating D_{waves}/D_j ratios typically well in excess of the 1.2 constant, typically closer to 1.6. This discrepancy is attributed to the fact that the water jets in use here are far smaller than Tatsuno's spheres, on the order of millimeters in diameter rather than centimeters. Therefore, the width of the meniscus between the jet and pool plays a larger role in determining n_{waves}.

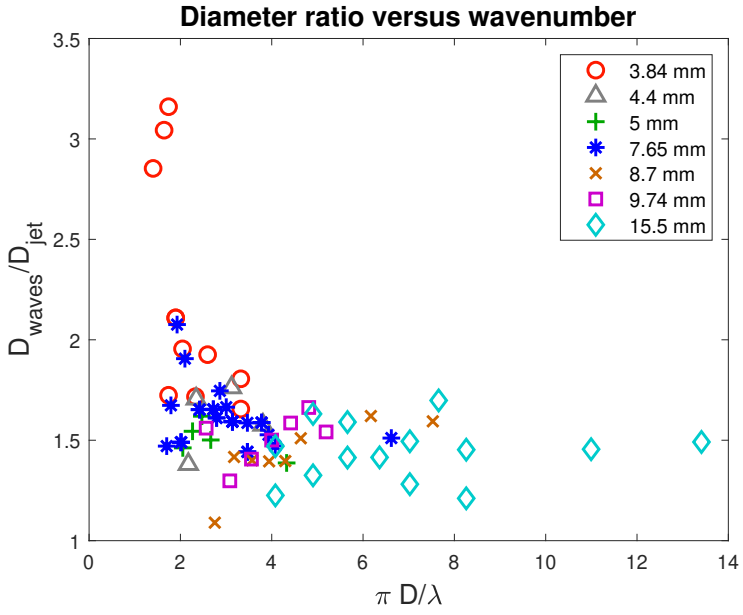

Figure 6. D_{waves}/D_j ratio for all jet ratios. Note general decreasing trend of diameter ratio with greater diameters. The horizontal axis $\pi D/\lambda$ is a nondimensionalization of the subharmonic waves' wavelength originally used by Tatsuno et al. (1969)

At some critical driving amplitude at a given frequency, the concentric waves that emit from the meniscus around the jet impact point destabilize over several jet disturbance cycles, transitioning to the subharmonic azimuthal wave behavior. It is believed that the waves grow exponentially from a minute perturbation after a small number of forcing cycles have occurred; at some time delay after this, they become large enough to be visible, before eventually saturating at some steady-state amplitude corresponding to the strength of the harmonic jet forcing. This time delay, based on qualitative observations, was found to fall in the region of 0.1-0.4 seconds. Shen & Liu (2020)

ascertained that the subharmonic, azimuthal waves are driven by the concentric waves, and they extended their analysis of body-driven azimuthal waves to the case of a cylinder that expands and contracts radially, much like our forced jet.

Tatsuno et al. (1969) observed that the disturbance amplitude at which the azimuthal waves transition from a concentric shape to the radial azimuthal wave form varies with the driving frequency. Particularly, they found that this concentric-radial transition amplitude decreases nonlinearly with frequency, changing greatly at lower frequencies, but less so at higher frequencies. Additionally, the required disturbance amplitude for wave transition depends much more strongly on frequency than it does on the wave ring diameter, with all inception conditions falling along a narrow range of curves. Fig. 7 illustrates these curves, which Tatsuno et al. likened to the shape of a rectangular hyperbola, when plotted on linear rather than logarithmic axes. Our jet-driven waves exhibit much the same behavior, with a clear dependence on driving frequency apparent in the size of the jet disturbances required for wave transition, as well as smaller variation in the onset conditions based on jet diameter.

For the case of the jet disturbances, we define the disturbance amplitude as the difference between the forced jet's maximum and minimum diameters:

$$a = D_{\mathrm{j,max}} - D_{\mathrm{j,min}} \tag{5}$$

And using such a definition of disturbance amplitude, we will designate the critical jet disturbance for wave transition from concentric to radial or azimuthal waves as $a_{\mathrm{C\text{-}R}}$, borrowing the nomenclature of Tatsuno et al. (1969).

It should be noted that, when nondimensionalized against the jet diameter, as well as the subharmonic gravity-capillary wavelength, our wave transition forcing amplitudes seem low compared to those of Tatsuno et al. One possibility for this discrepancy arises from the results of Fig. 6; broadly speaking, our $D_{\mathrm{waves}}/D_{\mathrm{j}}$ ratios are well above the value of 1.2 reported by Tatsuno et al. (1969) and Shen & Liu (2020). Assuming that the same mechanism is at play that transmits energy from the sphere or jet forcing into the water waves, our $D_{\mathrm{waves}}/D_{\mathrm{j}}$ ratios should be more in line with the 1.2 constant. However, Figures 6 and 7 do not consider the width of the meniscus that surrounds the jet. Because the jet velocity is relatively low, it does not draw the free surface around it downwards; rather, it meets with it smoothly by way of a meniscus around the perimeter of the jet. This meniscus extends outwards from the jet by a few millimeters, and it is this meniscus, rather than the jet sides, that interact with the water waves. We can characterize the size of this meniscus with the capillary length scale L_{c}, defined as:

$$L_{\mathrm{c}} \equiv \sqrt{\frac{\sigma}{\rho g}} \tag{6}$$

In the case of water, this length equals approximately 2.7 mm. Because our jets are only a matter of millimeters across, the addition of 2.7 mm in additional diameter from the meniscus is a significant

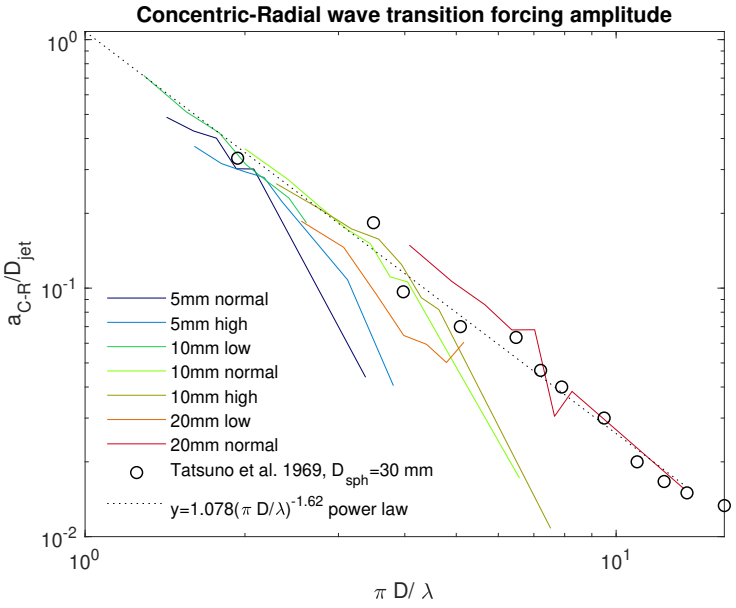

Figure 7. Observed wave concentric-radial wave transition forcing amplitudes, for several jet diameters. The data of Tatsuno et al. (1969), specifically the wave transition trend for their 30 mm sphere, were also included. The horizontal axis is nondimensional, using the gravity-capillary wavelength of the subharmonic waves, and the relevant jet or sphere diameter. For the sake of simplicity, we will refer to the critical disturbance amplitude for wave transition as Tatsuno et al. did, $a_{C\text{-}R}$.

fraction of D_j, while the spheres that Tatsuno et al. used were large, on the order of 30-60 mm, resulting in a much weaker, or negligible, impact of the capillary length. Thusly, it may be unfair to compare our results to those of Tatsuno et al. in this way. To try and rectify this, we may choose to include the added impact of L_c, replacing the diameter scale D_j with $D_j + L_c$. For convenience, we will refer to this as the compensated diameter, D_c:

$$D_c \equiv D_j + L_c \tag{7}$$

Fig. 8 demonstrates that that the D_c treatment collapses the jet-driven wave transition data quite effectively. Because of the close agreement by the transition amplitude values when plotted in this way, Tatsuno et al. proposed that a single function can predict the transition amplitude as a function of wavelength:

$$\frac{a_{C\text{-}R}}{D} = S\left(\frac{\pi D}{\lambda}\right) \tag{8}$$

Guessing that this function takes the form of a power law, it becomes:

$$\frac{a_{C\text{-}R}}{D} \propto \left(\frac{\pi D}{\lambda}\right)^{c_1} \tag{9}$$

Using a log-log plot, such as in Fig. 8, it is straightforward to determine c_1. With both D_j-referenced and D_c-referenced data in Fig. 8 collapsing into power law trends, the form of Eq. 9 appears well-

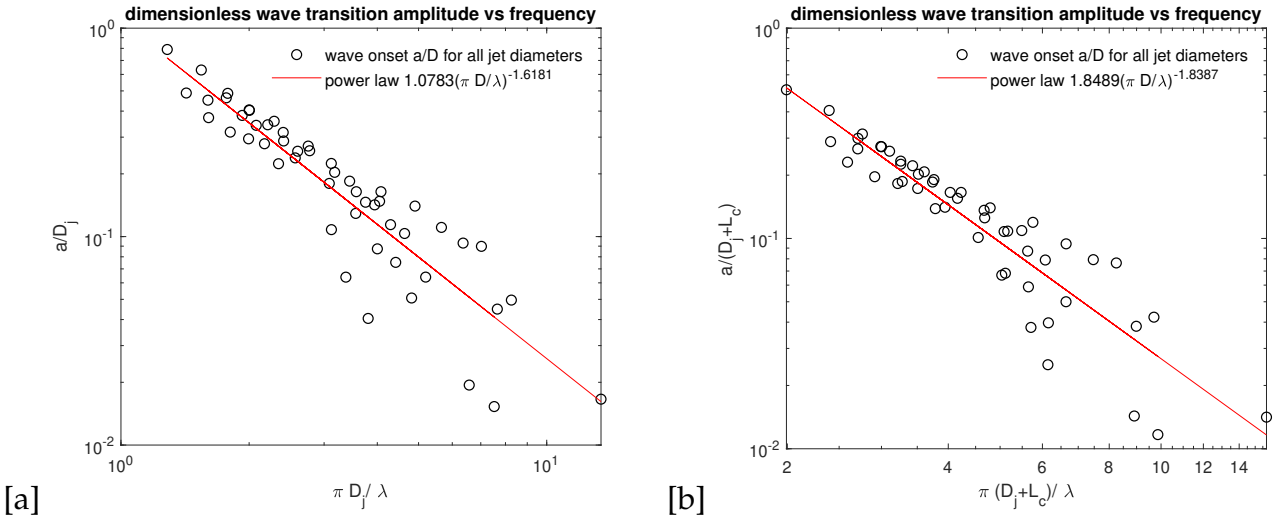

Figure 8. $a_{C\text{-}R}/D$ versus dimensionless wavenumber $\pi D/\lambda$, for selected jet cases. (a) $D=D_j$ (b) $D=D_j - L_c$

justified. Furthermore, Fig. 7 demonstrates that their results closely match our own, enabling us to use Eq. 10 as a more universal description for azimuthal wave onset. To apply this universal trend, we may use a regression to determine the coefficients c_0 and c_1 in Eq. 10:

$$\frac{a_{C\text{-}R}}{D} \approx c_0 \left(\frac{\pi D}{\lambda_{f/2}} \right)^{c_1} \tag{10}$$

Where $a_{C\text{-}R}$ is the forcing amplitude (in units of length) and $\lambda_{f/2}$ is the free surface wavelength corresponding to half of the forcing frequency. The specific values of the constants c_0 and c_1 were found to vary depending on whether the relevant diameter employed was D_j or D_c; the constants for D_c, because of the nature of that diameter scale, are more likely to fit the results of hard sphere experiments such as those of Tatsuno et al. (1969) or Taneda (1991). These coefficients are tabulated in Table 2. On the other hand, the constants corresponding to D_j are more likely to fit any hypothetical future investigations that use forcing bodies with diameters on the order of 5-10 millimeters, such as our liquid jets.

Table 2. Fit parameters for the concentric-radial (C-R) wave transition amplitude, using both the jet diameter D_j and the equivalent hard sphere diameter D_c. For diameters smaller than approximately 10 mm, the coefficients for D_j rather than D_c should be used, in order to compensate for the effect of the meniscus width.

	$D=D_j$	$D=D_c$
c0	1.08	1.85
c1	-1.62	-1.84

Once the waves have appeared, further increase in forcing intensity will result in the waves strengthening, with higher peaks and lower troughs. At a critical wave intensity, air entrainment will begin, as wave troughs descend far enough beneath the mean free surface height that they interact with

the subsurface jet flow. This jet flow contains strong convective accelerations, as well as vorticity production and vortex shedding events, and can develop regions of low pressure as a result. Sufficiently deep wave troughs can get pulled in by this pressure gradient, and they are stretched and expanded into bubbles that separate from the free surface and are advected deeper into the bulk by the jet flow, demonstrated in Fig. 9.

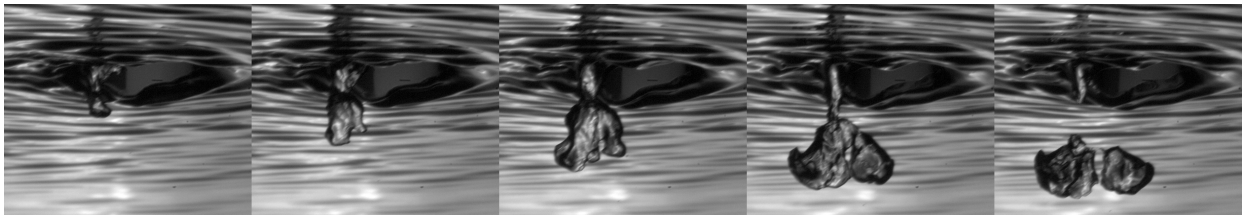

Figure 9. Entrainment of a single bubble by azimuthal waves, filmed from below water. At left, a single wave trough is initially drawn downwards. As time progresses, the bubble is first inflated, then pinched off, by the submerged jet flow.

There are two factors at play that might alter the size of the bubble, and therefore the ability of the forced jet to entrain air. One is the size of the waves; smaller, shallower waves are less likely to get caught by the subsurface flow, and larger, deeper ones are more likely. The other is the strength of the subsurface flow itself, a function of the jet's velocity; a higher impact velocity will result in greater convective accelerations near to the surface, and therefore a stronger pressure gradient to draw in the bubbles. There have so far been several investigations revealing how air entrainment increases with the size of jet disturbances, most notably the work of Zhu et al. (2000), and Davoust et al. (2002), who investigated entrainment by single large disturbances and partly controlled small disturbances respectively. Intuitively, entrainment by azimuthal waves should be no different. Thusly, it is useful to attempt to determine a functional dependence of air entrainment inception on the various physical parameters involved.

We suppose that air entrainment in this mode is controlled by competing forces of surface tension and subsurface suction. That is to say, the submerged jet flow and jet disturbances attempt to draw the bubbles down far enough to get captured as in Fig. 9, while the surface tension attempts to resist this, striving to minimize the interfacial surface area. As the bubble expands and pinches off, this represents the jet disturbances and jet flow overcoming the surface tension. To attempt to represent this, we propose a nondimensional pressure ratio, comparing the jet's dynamic pressure to the Laplace pressure associated with the surface waves that get captured and cause entrainment. To characterize the ability of surface tension to alter entrainment, we assume that the characteristic length of this Laplace pressure is equal to, or at least proportional to, the wavelength of the surface waves, giving this pressure ratio as:

$$\frac{P_{\text{dynamic}}}{P_{\text{capillary}}} = \frac{\rho U_j^2 \lambda_{f/2}}{\sigma} \tag{11}$$

Where $\lambda_{\text{f}/2}$ is the angular wavelength of the subharmonic surface waves, at half of the jet frequency f. However, this neglects the jet disturbance size a, a factor which is known to be important in

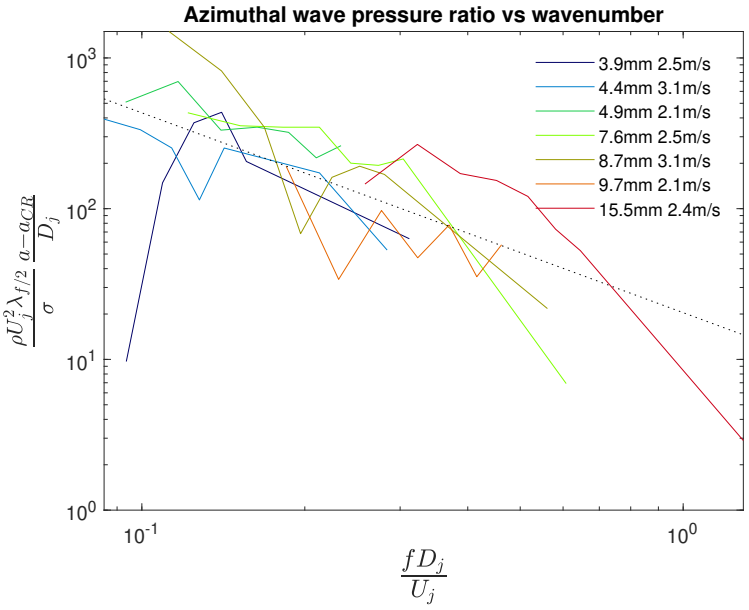

Figure 10. The pressure ratio P* at onset of air entrainment by azimuthal waves, versus forcing frequency normalized by jet velocity and diameter.

air entrainment. To accommodate this, we include $a - a_{\text{C-R}}$ normalized by the jet diameter D_j, a parameter which we presume to be a reasonable stand-in for the wave amplitude:

$$P^* \equiv \frac{\rho U_j^2 \lambda_{f/2}}{\sigma} \frac{(a - a_{\text{C-R}})}{D_j} \tag{12}$$

It can be seen in Fig. 10 that the pressure ratio P* at entrainment inception varies from approximately 10-1000 depending on the forcing frequency and jet diameter; however, a clean collapse onto a single curve is lacking, unlike the trend of forcing amplitude for concentric-radial wave transition. On the other hand, employing the same a/D_j versus $\pi D/\lambda$ as Fig. 7 seems to perform just as well, if not better, in Fig. 11. Therefore, it may be simplest to give the required forcing intensity for entrainment as a scalar multiple of the wave transition forcing intensity. On average, the forcing required for entrainment was approximately 25% greater than that for wave transition, so we could simply say $a_{\text{entrain}} = 1.25 * a_{\text{C-R}}$. However, while accurate, this criterion for air entrainment onset lacks any dependence on jet velocity, a factor that is assumed to be important; as such, we still desire a trend for entrainment onset based on P^*_{entrain}:

$$P^* \equiv \frac{\rho U_j^2 \lambda_{f/2}}{\sigma} \frac{(a - a_{\text{C-R}})}{D_j} \approx 20.4 * \left(\frac{fD_j}{U_j} \right)^{-1.32} \tag{13}$$

While P* does not perform very well in characterizing the air entrainment inception, its inclusion here is justified in that it attempts to bring a physical argument for air entrainment into an otherwise empirical matter. In this sense, we may use Fig. 10 to infer a lower bound for values of P* that will result in air entrainment; on the order of 50-400, depending on forcing frequency.

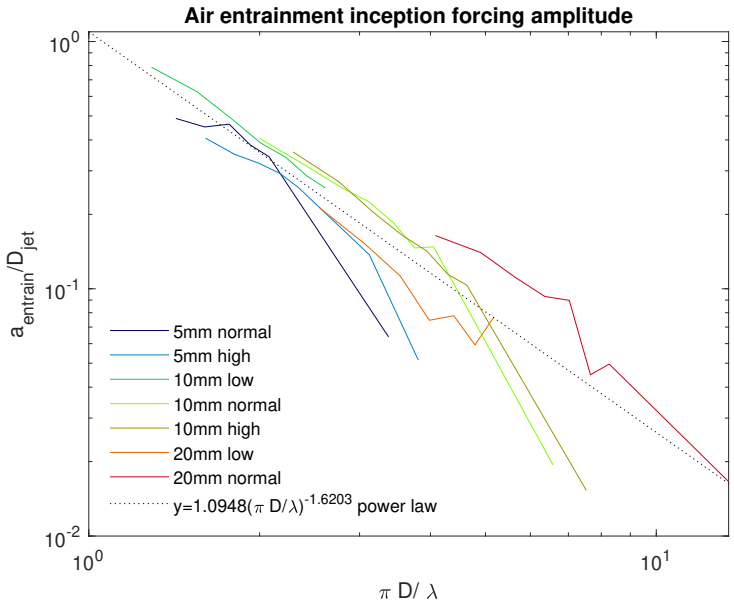

Figure 11. The diameter-normalized forcing intensity for air entrainment, versus dimensionless wavenumber. The same trend as in Fig. 7 is observed, albeit at slightly higher amplitude.

With the onset of air entrainment characterized, we now turn our attention to the volumetric flow rate of entrained air, at higher forcing values, when a exceeds $a_{entrain}$, and we continue to employ P*, using it now to characterize the volumetric flow rate. For the volumetric flow rate trials, six jet diameter/jet velocity cases were selected, and with each case, three different forcing frequencies were used; 60 Hz, 90 Hz, and 120 Hz. Four different forcing intensities were used at each jet diameter/frequency combination, ranging from slightly above air entrainment inception up until the higher-amplitude entrainment mechanism first described in depth by Zhu et al. (2000) was about to appear.

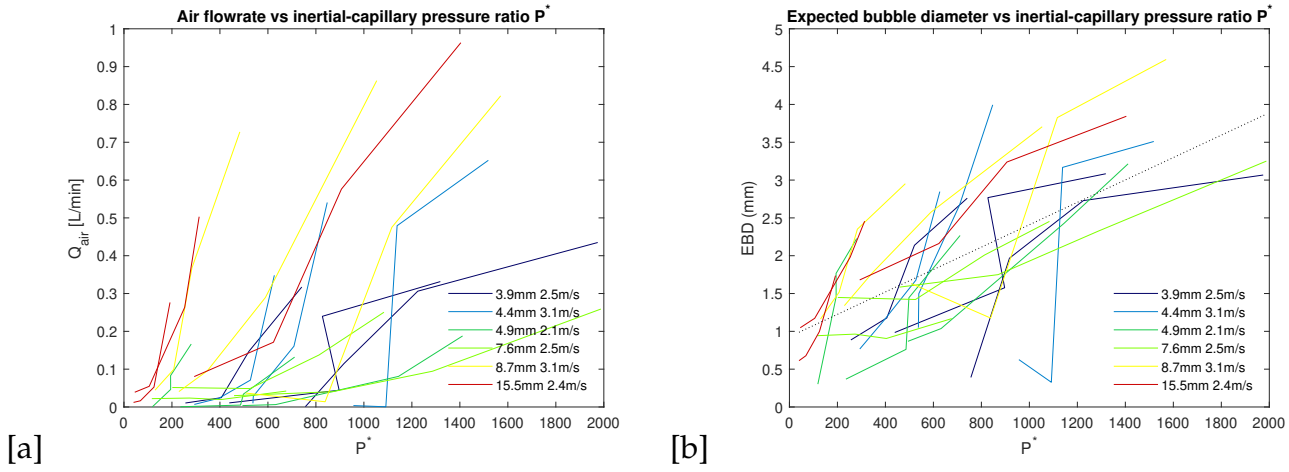

Figure 12. (a) Volumetric entrained air flow rate versus pressure ratio P*. (b) Expected bubble diameter versus pressure ratio P*.

In Fig. 12a, results from the broader air entrainment study are plotted against their corresponding

P^* values. A strong dependence on P^* is clear, likely due to its inclusion of the forcing intensity; however, there is a great deal of vertical and horizontal scatter in Q_{air} and P^*. Some of this can be immediately explained by remembering that air entrainment events only occur as the waves reach their peak amplitude, and that air entrainment always stems from one of the wave troughs. Additionally, in the case of a harmonic forcing imposed upon the jet flow such as this, vorticity roll-up and shedding in the submerged jet region are likely to ultimately occur at the frequency of the forcing (Becker & Massaro, 1968). Intuitively, this means that higher frequency waves and wave rings with a greater value of n_{waves} should be relatively more effective at entraining air. We can correct for this effect by inventing an "effective bubble diameter", that is, the size of air bubble that would be entrained if every single wave trough with every single jet cycle entrained a bubble of the same size, assuming that every hypothetical bubble entrained is spherical. This is given by:

$$\text{EBD} \equiv \left(\frac{6Q_{\text{air}}}{\pi f n_{\text{waves}}} \right)^{1/3} \tag{14}$$

The expected bubble diameter collapses vertically reasonably well in Fig. 12b; for every case, entrainment starts at an EBD of approximately 0.5-1 mm, and every case tops out around 2.5-4 mm, depending on various parameters. By the time the EBD reaches approximately 3-4 mm, the jet disturbances are strong enough to entrain air by means that do not require azimuthal waves, namely the mechanism reported by Zhu et al. (2000), wherein large jet disturbances form deep axisymmetric craters in the pool that collapse to entrain a large annular bubble. With the definition of the expected bubble diameter removing much of the scatter seen in Fig. 12a, it becomes apparent in Fig. 12b that EBD appears to vary approximately linearly with P^*, likely because the pressure ratio is referenced against the excess forcing $a - a_{\text{C-R}}$, meaning that it must equal zero when no air is entrained. A first guess at capturing this dependence of the expected bubble diameter on the pressure ratio might be to apply a linear fit, seen as the dotted black line in Fig. 12b:

$$\text{EBD (mm)} \approx 0.93 + 0.0015P^*, \quad 0.5 < \text{EBD} < 4 \tag{15}$$

This is a loose fit, and it should be noted that this slope varies somewhat with parameters like jet velocity and jet diameter. However, for several cases, EBD appears to scale approximately linearly with P^*. Accordingly, we propose that the volumetric flow rate of entrained air is a function of the wave mode number, forcing frequency, excess disturbance a^*, fractional disturbance a/D_j, and jet velocity U_{jet}:

$$\begin{aligned} Q_{\text{air}} &= Q_{\text{air}} \left(f, n_{\text{waves}}, P^*, \frac{a}{D_j}, U_j \right) \\ Q_{\text{air}} &\propto f n_{\text{waves}} \left(0.93 + 0.0015P^*\right)^3 (U_j)^{\gamma_1} \end{aligned} \tag{16}$$

Here, γ_1 is assumed to be a positive constant, to capture the dependence of Qair on the jet velocity. By defining P^* as in Eq. 12, we suppose that the jet's dynamic pressure controls the ability of

the subsurface flow to overcome surface tension and draw wave troughs downwards to cause entrainment events. It therefore seems reasonable to conclude that γ_1 should equal 2, assuming that the EBD scales directly with the dynamic pressure.

So far, details of the interactions between the surface waves and the submerged jet flow, and subsequent air entrainment events, have only been guessed at; closer inspection of the problem is accordingly required to gain a more complete understanding. Central to these interactions is the pulsatile nature of the jet forcing; such matters have been investigated before, particularly in the experiments of Becker & Massaro (1968) and Ma et al. (2022), but these experiments imposed an external acoustic forcing, and a fluctuating velocity condition, respectively. This differs somewhat from the plunging jet case, where viscous action in the column of water falling from the nozzle renders its velocity largely constant, with the nozzle's velocity perturbations becoming fluctuations in the diameter of the jet.

In both of these past experiments, the submerged jet required some distance, on the order of 2-4 jet diameters downstream, for Kelvin-Helmholtz vortices and their related entrainment events to grow. The growth of these vortices, and their connection to a fluctuating jet core, has been found to influence mixing in the submerged jet, as the fluctuating diameter of the jet downstream of its outlet is coupled to entrainment of ambient fluid. We believe that these events, where Kelvin-Helmholtz vortices draw the relatively quiescent ambient fluid in to the jet, are what capture bubbles from the surface waves; investigation of the results of Ma et al. (2022) reveals ambient fluid entrainment at points where the diameter of the jet core is at its minimum, and this timing is reflected by the plunging jet as well, with entrainment events typically initiating as the jet reaches its minimum diameter.

There is one caveat, however; as mentioned before, such events require a finite jet development length to occur, but as demonstrated in Fig. 9, air entrainment occurs close to the surface, within 1 jet diameter of the plunge point. This implies one of two things; either that a submerged jet with a fluctuating inflow diameter, rather than velocity, entrains ambient fluid more vigorously and sooner than one with a fluctuating inflow velocity, or that the strong pressure gradient that captures bubbles is from a different source entirely. To answer these questions, quantitative velocity measurements in the submerged jet would likely be required.

4. Conclusions

Here, a novel air entrainment mechanism by a disturbed plunging jet has been presented. While the present understanding of the azimuthal wave mechanism is rigorous, having been explored previously by several investigators, there has been little investigation of the interaction of azimuthal waves with the subsurface flow, and before this work, none whatsoever concerning the ability of these subharmonic waves to entrain air (Taneda, 1991). It has been found that the concentric-radial transition of these azimuthal waves may be predicted approximately as a power law dependence on the nondimensional wavenumber:

$$\frac{a_{\text{C-R}}}{D_{\text{c}}} \approx 1.85 * \left(\frac{\pi D_{\text{c}}}{\lambda_{f/2}}\right)^{-1.84} \tag{17}$$

It has been found that Eq. 17 not only predicts onset of the jet-driven azimuthal waves, but also performs quite well for the results of Tatsuno et al. (1969). The azimuthal wave mode number n_{waves} may be determined by the gravity-capillary dispersion relation, as well as the ratio between the diameter of the wave ring and the diameter of the jet. For large bodies, this ratio is approximately 1.2, though for smaller jets, it grows to 1.6-2 as the impact of the meniscus becomes greater:

$$n_{\text{waves}} = \frac{D_{\text{waves}}}{D_{\text{j}}} k_{f/2} r_{\text{j}} \tag{18}$$

This work has revealed that in the case of a harmonically forced plunging jet, at a small increment of forcing intensity above this transition amplitude, the waves will begin to entrain air. This transition amplitude, at higher frequencies (above approximately 30-70 Hz, depending on jet diameter and velocity), is substantially lower than that which would be required for entrainment in the fashion documented by Zhu et al. (2000); in the case of forcing amplitude being slowly increased for a given frequency, entrainment by azimuthal wave will occur first, and then, at a higher critical amplitude, roughly corresponding to an expected bubble diameter of 4 mm, the high-amplitude axisymmetric air entrainment would begin. The flow rate of that air entrainment is suspected to be a function of a number of parameters, namely the forcing frequency, azimuthal wave mode number, excess disturbance, jet diameter, and jet velocity, but the available data makes it clear that the most influential factor in determining Q_{air} is still the disturbance amplitude of the jet a, as demonstrated in Fig. 12b and outlined by Eq. 16.

The dependence of the entrained air flow rate on the jet forcing frequency and intensity is expected to vary in several ways; most notably, it is concluded that higher frequency forcing is relatively more effective at entraining air, since opportunities for air entrainment events occur more frequently. However, the size of the jet disturbances appears to affect air entrainment in two regards; firstly, larger jet disturbances lead to a larger azimuthal wave amplitude, though it is likely that the amplitude of these waves eventually saturates. Secondly, the jet disturbances are believed to alter the subsurface flow, prompting Kelvin-Helmholtz roll-up at the forcing frequency; the corresponsing evolution of the submerged jet flow then influence bubble entrainment. However, the complex interplay between surface phenomena and subsurface flow will need to wait until velocimetry studies can be carried out.

Acknowledgements

This work was supported by the DLA-Troop Support, Philadelphia, PA and the Defense Logistics Agency Information Operations, J68, Research & Development, Fort Belvoir, VA under contract SP4701-18-D-1200.

Nomenclature

a	Jet disturbance amplitude [mm]
$a_{\text{C-R}}$	Critical disturbance amplitude for azimuthal wave onset [mm]
a_{entrain}	Critical disturbance amplitude for air entrainment inception [mm]
a^*	Excess disturbance
D_0	Original jet diameter [mm]
D_j	Jet diameter at impact [mm]
D_{c}	Capillary length-compensated jet diameter at impact [mm]
D_{sph}	Diameter of a surface-piercing forcing sphere [mm]
D_{waves}	Diameter of azimuthal wave ring [mm]
EBD	Expected bubble diameter [mm]
f	Forcing frequency [Hz]
$k_{f/2}$	Angular wavenumber of water waves at $1/2f$ [rad-m^{-1}]
L_c	Capillary length scale [mm]
L_j	Jet fall height [mm]
$\lambda_{f/2}$	Wavelength water waves at $1/2f$ [m]
n_{waves}	Azimuthal wave mode number
P^*	Dynamic/capillary pressure ratio
Q_{air}	Volumetric entrained air flow rate [m^{3}s^{-1}]
ρ_a	Air density [kg m^{-3}]
ρ, ρ_w	Water density [kg m^{-3}]
σ	Surface tension [N m^{-1}]
U_0	Jet velocity at nozzle mouth [m s^{-1}]
U_j, U_{jet}	Jet velocity at impact [m s^{-1}]

References

Becker, H. A., & Massaro, T. A. (1968). Vortex evolution in a round jet. *Journal of Fluid Mechanics*, *31*(3), 435448. doi:

Davoust, L., Achard, J.-L., & El Hammoumi, M. (2002). Air entrainment by a plunging jet: the dynamical roughness concept and its estimation by a light absorption technique. *International Journal of Multiphase Flow*, *28*(9), 1541–1564.

Ma, X., Gong, X., & Jiang, N. (2022). Experimental study of vortex formation in pulsating jet flow by time-resolved particle image velocimetry. *Physics of Fluids*, *34*(3), 035105. Retrieved from `https://doi.org/10.1063/5.0084536` doi:

Moisy, F., Rabaud, M., & Salsac, K. (2009). A synthetic schlieren method for the measurement of the topography of a liquid interface. *Experiments in Fluids*, *46*(6), 1021–1036.

Morel, T. (1975). Comprehensive design of axisymmetric wind tunnel contractions.

Ridgeway, C. D., Ripplinger, K., Detwiler, D., & Luo, A. A. (2020). Prediction of entrained oxide inclusions and oxide induced defects during directional flow in aluminum casting. *AFS Trans*, *128*.

Shen, M., & Liu, Y. (2020). Instability of finite-amplitude gravity–capillary progressive ring waves by an oscillating surface-piercing body. *Journal of Fluid Mechanics*, *887*.

Taneda, S. (1991). Visual observations of the flow around a half-submerged oscillating sphere. *Journal of fluid mechanics*, *227*, 193–209.

Tatsuno, M., Inoue, S., & Okabe, J. (1969). Transfiguration of surface waves. *Rep. Res. Inst. Appl. Mech. Kyushu University*, *17*, 195–215.

Zhu, Y., Oğuz, H. N., & Prosperetti, A. (2000). On the mechanism of air entrainment by liquid jets at a free surface. *Journal of Fluid Mechanics*, *404*, 151–177.